Comprehensive Analysis Aeroelastic Stability Predictions for the Mars Sample Recovery Helicopters and Ingenuity

Stephen J. Wright
Aerospace Engineer
NASA Ames Research Center
Moffett Field, California, USA

Gianmarco Sahragard-Monfared
Aerospace Engineer
NASA Ames Research Center
Moffett Field, California, USA

Natasha L. Schatzman
Aerospace Engineer
NASA Ames Research Center
Moffett Field, California, USA

Wayne Johnson
Aerospace Engineer
NASA Ames Research Center
Moffett Field, California, USA

Paulina Ridland
Aeromechanical Engineer
AeroVironment, Inc.
Simi Valley, California, USA

Michael Fillman
Aeromechanical Engineer
AeroVironment, Inc.
Simi Valley, California, USA

ABSTRACT

A rotorcraft comprehensive analysis was used to generate aeroelastic stability predictions for both Ingenuity and the Mars Sample Recovery Helicopters. The analysis was performed multiple times for each rotor system with sequential increases to the level of modeling complexity. Initial cases used an independent blade analysis, trim inflow distribution, no airframe degrees of freedom, and a hover condition (a time-invariant problem). The final model used all blades, dynamic inflow, airframe rigid body degrees of freedom, and a Floquet theory approach to the flutter analysis. The approach of sequentially increasing modeling complexity was employed to ensure the causes of any observed instabilities could be identified. For each case, stability results were determined across a range of air densities, tip Mach numbers, and rotor collective pitch settings. For the Sample Recovery Helicopter, a forward flight condition analysis with the highest level of modeling complexity was also performed. The aeroelastic stability predictions showed both the Ingenuity and Sample Recovery Helicopter rotor systems to be stable for all analyzed conditions. Parameter excursions of structural properties were performed to explore conditions resulting in aeroelastic instabilities.

NOTATION

A	Disk area, m^2
C_T	Thrust coefficient, $T/\rho A V_{tip}^2$
M_{tip}	Tip Mach number
T	Thrust, N
V_{tip}	Tip speed, m/s
θ_{75}	Collective pitch, defined at 75% radius, deg
ρ	Air density, kg/m^3
σ	Thrust-weighted solidity

INTRODUCTION

Ingenuity has executed over seventy flights on Mars to date (Ref. 1) and has demonstrated the feasibility of using helicopters for future Mars missions, including for the planned Mars Sample Return campaign (MSR). MSR currently includes two "Ingenuity-class" helicopters to assist with the retrieval of soil sample tubes (Ref. 2). As illustrated in Figure 1, the baseline concept for each Sample Recovery Helicopter (SRH) relies on heritage from the Ingenuity design, but in addition to component and software/avionics upgrades, each also includes wheels for ground mobility and a robotic arm for sample tube manipulation (Refs. 2 and 3).

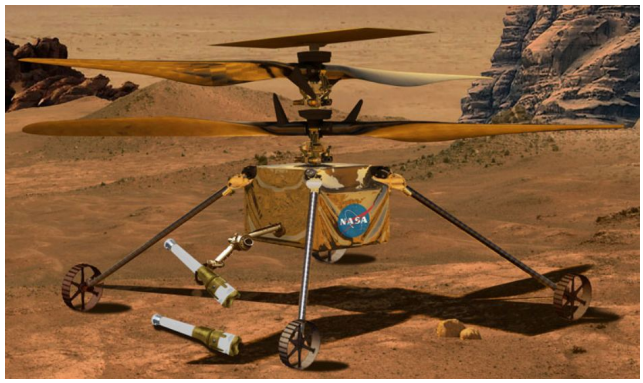

Figure 1. Mars Sample Recovery Helicopter configuration (Ref. 2).

While the baseline SRH rotor design relies heavily on heritage elements from the Ingenuity design, it is sufficiently different to necessitate new aeroelastic stability analysis. For the present work, Comprehensive Analytical Model of Rotorcraft Aerodynamics and Dynamics (CAMRAD II) (Ref. 4), a

Presented at the Vertical Flight Society's 6th Decennial Aeromechanics Specialists' Conference, Santa Clara, CA, Feb. 6-8, 2024.

rotorcraft comprehensive analysis tool, was used to generate aeroelastic stability predictions for both the SRH and Ingenuity in hover and for the SRH in forward flight. The analysis was performed with sequential increases to the level of modeling complexity. Initial hover cases used an independent blade analysis, trim inflow (which is not perturbed in the flutter solution), no airframe degrees of freedom (DOF), and a hovering operating condition so the linearized equations are time-invariant. The final hovering analysis and the SRH forward flight analysis included all blades, dynamic inflow, and airframe rigid body DOF, and used the Floquet theory (Ref. 5) approach to the flutter analysis. The approach of sequentially increasing complexity ensured the causes of any observed instabilities could be identified. Stability results were predicted for multiple air densities (ρ), tip Mach numbers (M_{tip}), rotor collective pitch settings (θ_{75}), and air speeds.

In addition to modeling and analyzing the SRH and Ingenuity rotors, analysis was performed for the SRH rotor with varied structural properties. The purpose of these excursions was to identify parameters of importance for stability of rotors designed for operating on Mars.

ROTOR MODELS

For analysis of the Ingenuity rotor, existing CAMRAD II models were used (Ref. 6), including previously calculated values for the structural properties of the rotor. To facilitate comparison with the SRH, the Ingenuity model was modified to exclude the counterweights near the blade roots. For the SRH rotor, a new CAMRAD II model was needed due to structural and geometric changes from Ingenuity's design. Table 1 summarizes key characteristics of the Ingenuity and SRH rotor models, and Figure 2 is a photo of an as-built SRH blade. Radius was increased for the SRH, but airfoils and their distribution along the radius were designed to match those of Ingenuity.

Table 1. Ingenuity and SRH Rotor Characteristics.

Parameter	Ingenuity	SRH
Radius, m	0.605	0.700
Thrust-weighted solidity (per rotor)	0.07391	0.06412
Design rotor speed, RPM	2600	2350

Sectional structural properties of the SRH blade were calculated via finite element method (FEM) at specific radial stations by AeroVironment, the organization that created the structural design for both Ingenuity and the SRH (Refs. 7-8).

The SRH and Ingenuity blades both consist of a foam core wrapped in carbon fiber. Both blades are reinforced with a series of upper and lower carbon fiber spar caps. As was the case with Ingenuity, the stiffness-driven SRH blade design was tailored to meet the regressing first flap frequency required to avoid excitation by the flight control system. This was achieved by modifying the spar layup through iterative FEM analysis and modal testing.

Figure 2. SRH prototype rotor blade
Credit: Langberg, S., AeroVironment, Inc.

Fan plots for the SRH and Ingenuity rotors are presented in Figure 3, with the SRH depicted by solid red lines and Ingenuity by dashed black lines. For the CAMRAD II SRH structural model, the root stiffness was tuned to match the non-rotating frequencies for the fundamental flap, lag, and torsion modes from FEM calculations. These frequencies are denoted by the symbols in Figure 3 (F1 = first flap, L1 = first lag, T1 = first torsion).

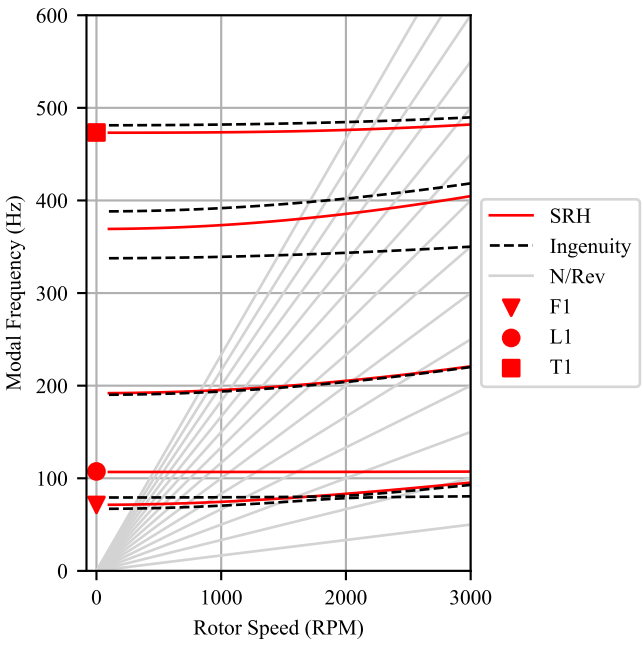

Figure 3. SRH and Ingenuity fan plots generated with CAMRAD II (hover, in vacuo, θ_{75} = 0 deg), non-rotating fundamental frequencies from FEM analysis marked with red symbols.

The twist and chord values used in the CAMRAD II models are depicted graphically in Figure 4.

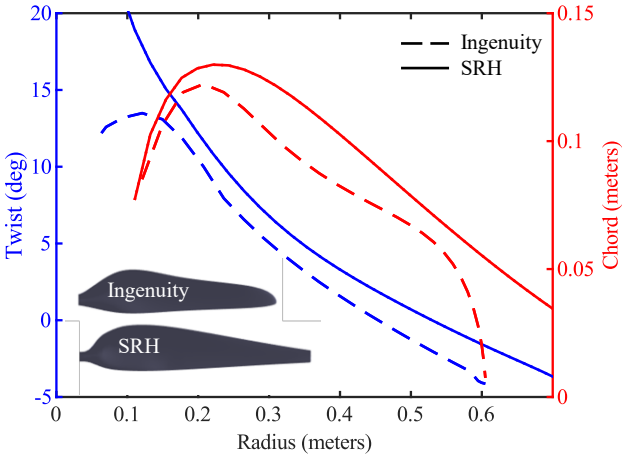

Figure 4. Twist and chord distributions vs blade radius for the SRH and Ingenuity rotor blades.

In the analysis, the rotors were trimmed using the CAMRAD II free wake model for coaxial rotors to account for the different thrusts of the upper and lower rotors in the coaxial configuration. A single set of airfoil tables (based on work in Ref. 6 and corresponding to Mars conditions at a density of 0.017 kg/m^3) was used for all the present calculations. The density variations examined in this work imply variation in Reynolds number, which affects the performance of the rotor, but the Reynold's number variation is not expected to affect the aeroelastic stability. Figure 5 shows the variation of blade loading, C_T/σ (average of the upper and lower rotors), with collective pitch.

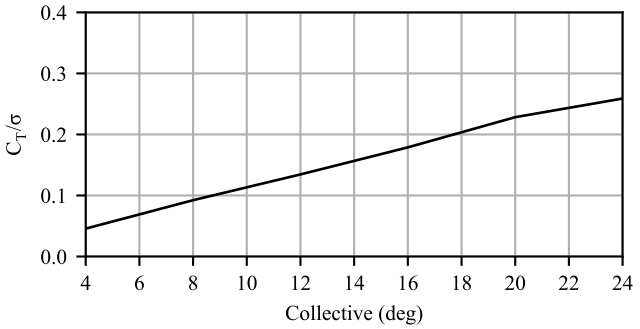

Figure 5. C_T/σ vs collective for the SRH, ρ = 0.013 kg/m^3, M_{tip} = 0.5.

It must be noted that after the commencement of the present work, minor changes were made to the blade geometry to maximize blade length that could be accommodated in the aeroshell. This growth is not captured in Table 1 or Figures 3-4, nor was it incorporated in any of the analysis presented in this document. The growth in radius is small (less than 1%) and is not expected to have a significant impact on the aeroelastic stability.

SRH HOVER RESULTS

This section is devoted to results of the SRH hover analysis. A subsection is devoted to each of the different levels of modeling complexity, and conclusions are drawn regarding the effects of the different modeling approaches on the stability predictions. The density, tip Mach number, and collective ranges investigated cover the current expected range of operating conditions of the SRH rotors on Mars. Cases were run for two densities: 0.013 and 0.020 kg/m^3. At each density, a collective pitch sweep was simulated with collective values ranging from 4 to 24 deg, and a tip speed sweep was simulated with M_{tip} values ranging 0.4 to 0.9. The collective value of 20 deg is high enough for the effect of stall to be evident in the rotor power, as indicated by Figure 6, a plot of figure of merit versus collective.

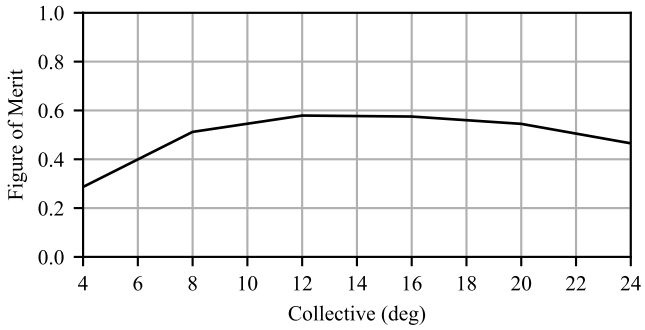

Figure 6. Figure of merit vs collective for the SRH, ρ = 0.013 kg/m^3, M_{tip} = 0.5.

As will be demonstrated for a single M_{tip} sweep in the first subsection, the 0.013 and 0.020 kg/m^3 SRH stability results are very similar. As such, after this demonstration case, only the 0.013 kg/m^3 cases are shown in the body of this paper. Results for the SRH simulations with 0.020 kg/m^3 density are presented in Appendix A.

The hover results and conclusions presented in the following sections are based on the analysis of the SRH rotor system. Ingenuity results were also generated. As will be demonstrated for a single M_{tip} sweep in the first subsection, the SRH and Ingenuity stability results are similar. Thus, except for this demonstration, only the SRH cases are shown in the body of this paper. Ingenuity results are included for completeness in Appendix B.

Regarding stability plots, given the method by which CAMRAD II outputs the eigenvalues and the method by which the values were parsed and plotted with connecting lines for each mode, there is the potential for the connection of data points to not accurately depict a single mode (mode crossings were not automatically captured). Some of the plots presented (though not all) include the manual reconstruction of the modes. It should be noted that the lines depicting modes are in some cases approximate, but that sufficient reconstruction has been performed to reveal the overall stability trends.

Independent Blade | Trim Inflow | No Airframe DOF Flutter Analysis: Constant Coefficient

The analysis for the present subsection used an independent blade for each rotor, trim inflow, no airframe degrees of

freedom, and a constant coefficient flutter analysis. Figures 7-8 present modal frequencies and damping ratios plotted against M_{tip} for two different collective settings. Damping ratio is defined as the negative real eigenvalue component divided by the magnitude of the eigenvalue. Positive damping ratios indicate stability. Lines of the same color are for the same mode; there are two lines per mode (one solid and one dashed) because there are two rotors. By the author's convention, for each mode, the line corresponding to the lower magnitude real eigenvalue component at the initial sweep condition is plotted as a solid line, while the other is plotted as a dashed line. In Figure 7, lines were labeled according to the mode shapes at the blade tip at M_{tip} = 0.4. F = flap, L = lag, T = torsion, and the number proceeding each letter denotes the number of the mode of that type. The Figure 7 labeling is assumed applicable for subsequent SRH plots in this subsection. The color-coded labeling can also be generally applied to the SRH constant coefficient results in Appendix A.

The rotor is stable for all speeds analyzed for Figures 7-8. With 10 deg collective, the damping ratios of the first flap mode increases noticeably with increasing tip speed. This trend is not as apparent with 20 deg collective. For both collective settings, the damping ratio of the first lag mode is the smallest and is relatively independent of tip speed.

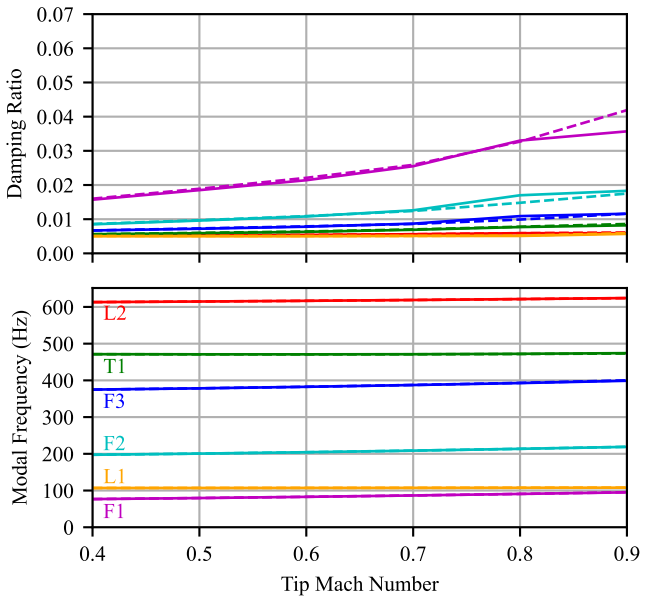

Figure 7. Modal frequency and damping vs M_{tip}, ρ = 0.013 kg/m^3, θ_{75} = 10 deg.

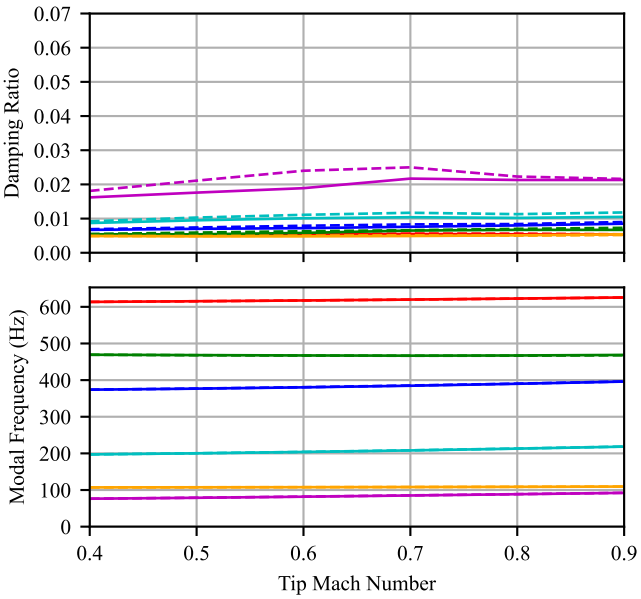

Figure 8. Modal frequency and damping vs M_{tip}, ρ = 0.013 kg/m^3, θ_{75} = 20 deg.

Figures 9-10 correspond to sweeps of collective for M_{tip} = 0.5 and M_{tip} = 0.8. Neither sweep exhibits instability, but stability of the first flap mode generally decreases with increasing collective. The damping ratios of several modes display notable dependence on rotor speed. In particular, the first flap mode has significantly higher damping at low collective with M_{tip} = 0.8 than with M_{tip} = 0.5.

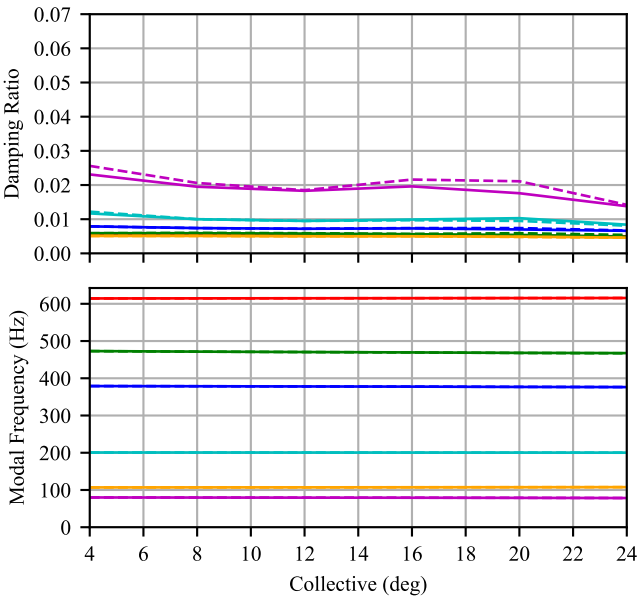

Figure 9. Modal frequency and damping vs collective, ρ = 0.013 kg/m^3, M_{tip} = 0.5.

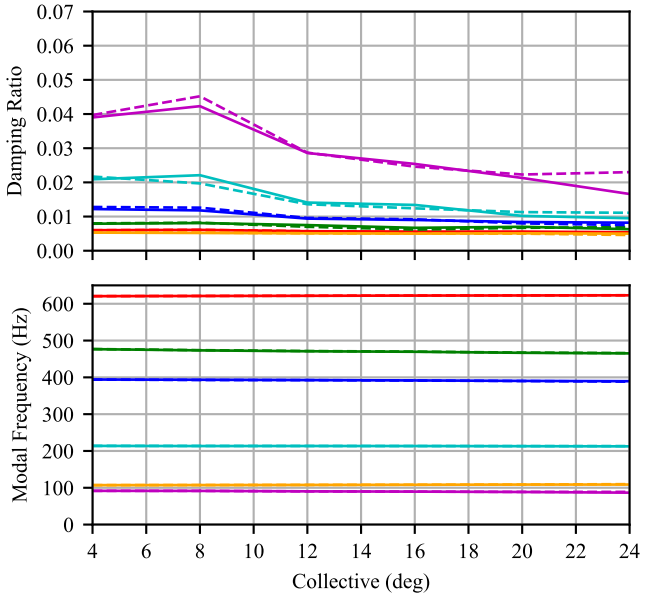

Figure 10. Modal frequency and damping vs collective, ρ = 0.013 kg/m^3, M_{tip} = 0.8.

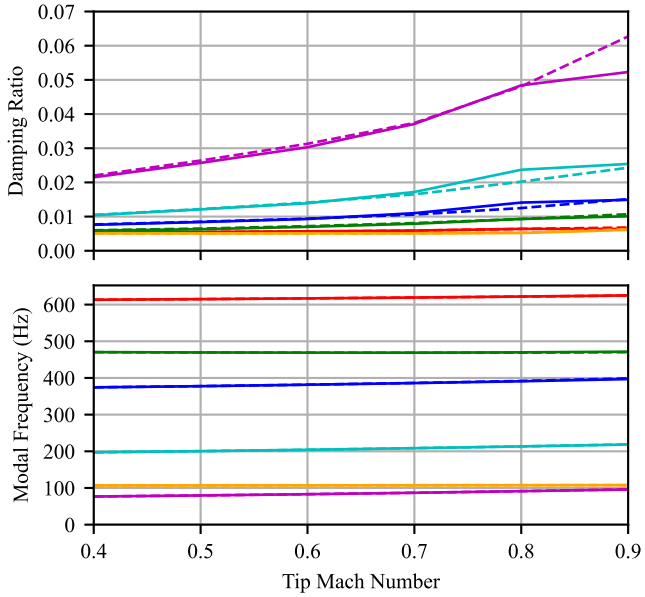

Figure 11. Modal frequency and damping vs M_{tip}, ρ = 0.020 kg/m^3, θ_{75} = 10 deg.

As previously discussed, the simulations were performed for both 0.013 and 0.020 kg/m^3 densities. The results are very similar, as demonstrated by comparing the 0.020 kg/m^3 results in Figure 11 with the 0.013 kg/m^3 results shown previously in Figure 7. While the higher density yields significantly higher damping for the first flap mode at higher tip speeds, the damping ratio trends for the two densities match closely. The frequency plots for the two densities are nearly indistinguishable from one another. Because of the similarity of the results, all other SRH results for 0.020 kg/m^3 are reported in Appendix A.

The hover simulations performed for the SRH rotor were also performed for the Ingenuity rotor. The stability results were similar, as demonstrated by a comparison of Figure 12 (Ingenuity) and Figure 7 (SRH). Comparing the damping results of the two rotors for these conditions, the trends are nearly identical. Because of the general similarity of the SRH and Ingenuity stability trends, for brevity, all other Ingenuity results are reported in Appendix B.

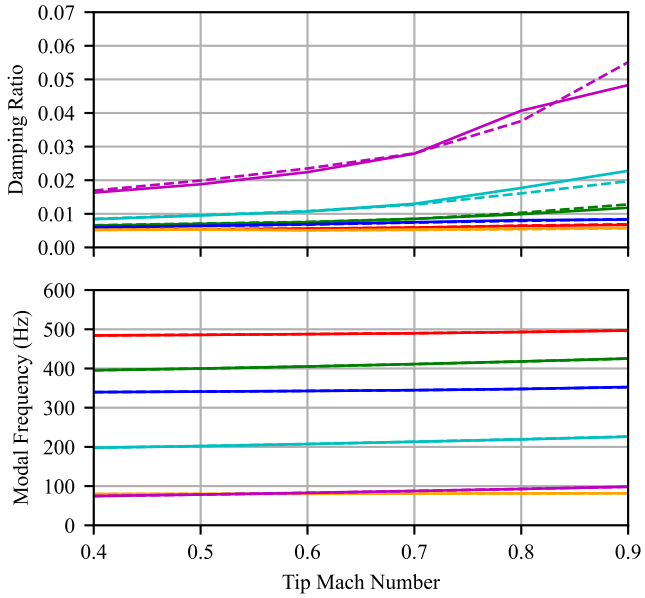

Figure 12. Ingenuity results: modal frequency and damping vs M_{tip}, ρ = 0.013 kg/m^3, θ_{75} = 10 deg.

The stability results from the constant coefficient flutter analysis have thus far been presented with plots of damping ratio, in which positive values indicate stability. With two-bladed rotors, coupling of blade motion with dynamic inflow or airframe motions introduces periodic coefficients in the linearized equations, as does the aerodynamics of forward flight. In all following sections, Floquet theory is used for the flutter analysis, capturing the periodic coefficients in the stability equations. For the Floquet theory results, stability is assessed via plots of real eigenvalue components, in which *negative* values indicate stability. To facilitate a comparison between the results of the two stability analyses, the stability results presented in Figures 7-10 are reproduced in Figures

13-16, but as plots of real eigenvalue components instead of damping ratios. As in the previous damping ratio plots, the stability of the first flap mode (magenta) increases with tip speed and decreases with collective, while the stability margin of the first lag mode (yellow) is the smallest of all modes and is relatively independent of tip speed and collective.

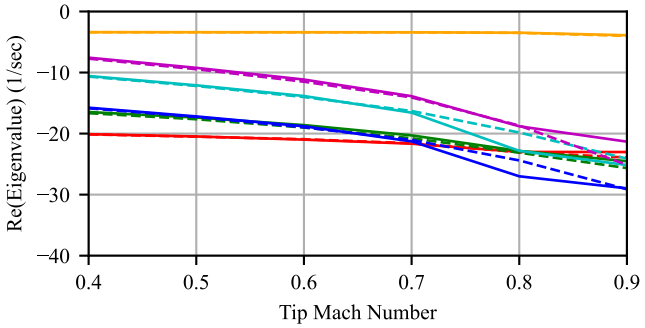

Figure 13. Real eigenvalue components vs M_{tip}, ρ = 0.013 kg/m^3, θ_{75} = 10 deg.

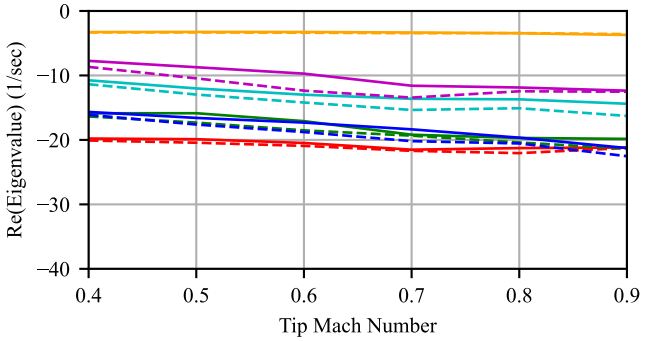

Figure 14. Real eigenvalue components vs M_{tip}, ρ = 0.013 kg/m^3, θ_{75} = 20 deg.

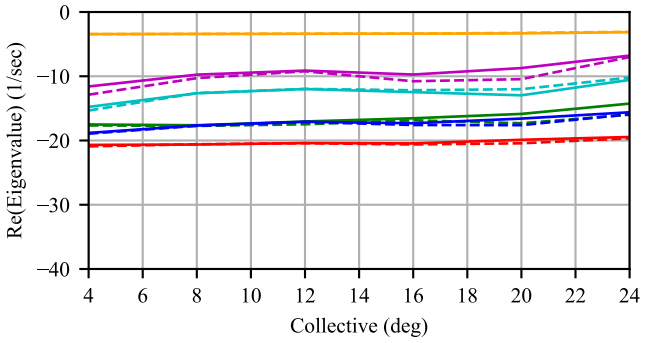

Figure 15. Real eigenvalue components vs collective, ρ = 0.013 kg/m^3, M_{tip} = 0.5.

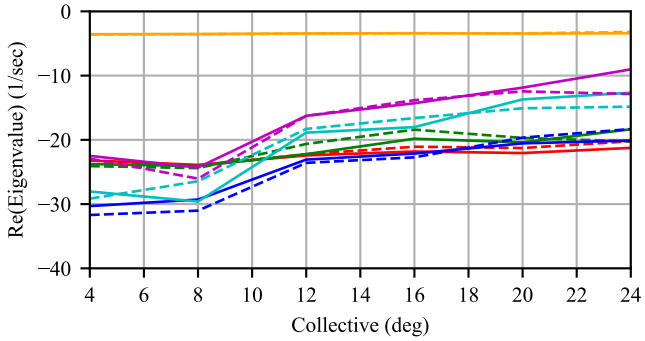

Figure 16. Real eigenvalue components vs collective, ρ = 0.013 kg/m^3, M_{tip} = 0.8.

Independent Blade | Trim Inflow | No Airframe DOF Flutter Analysis: Floquet Theory

The analysis of the previous section was repeated, with the only change being the method used for the flutter solution. In the previous section, a constant coefficient approximation of the periodic coefficients was used. In this section, Floquet theory was used. For all Floquet theory results, stability is plotted as the real components of the eigenvalues, with *negative* values indicating stability. As with the prior section, lines of the same color are for the same mode, the two rotors resulting in two lines per mode (one shown with a solid line and the other with a dashed line). For each mode, the line corresponding to the smaller magnitude real eigenvalue component at the initial sweep condition is plotted with a solid line, while the other is plotted with a dashed line.

Note that an attempt was made to plot modes with the same color, regardless of analysis type (e.g. the mode that is plotted in yellow for the constant coefficient results is the same mode as the mode that is plotted in yellow for the Floquet theory results). However, due to complexities deciphering the Floquet theory eigenvalue output and correcting for mode crossings, the coloring may in some cases be inconsistent.

Figures 17-18 show stability versus tip speed for two different collective settings: 10 and 20 degrees. The rotor is stable for the entirety of each sweep. As with the constant coefficient analysis of the previous subsection, most of the modes exhibit a general trend of increasing stability with blade tip speed. The trend is more significant for the cases with less collective pitch. As with the constant coefficient results, the stability margin of the minimally damped lag mode is relatively insensitive to tip speed and collective. Comparing Figures 17-18 with the eigenvalues of the time-invariant equations (Figures 13-14) confirms that the numerical integration of the state transition matrix is accurate.

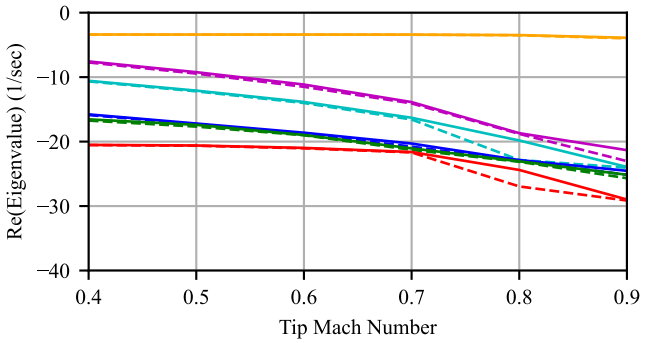

Figure 17. Real eigenvalue components vs M_{tip}, ρ = 0.013 kg/m^3, θ_{75} = 10 deg.

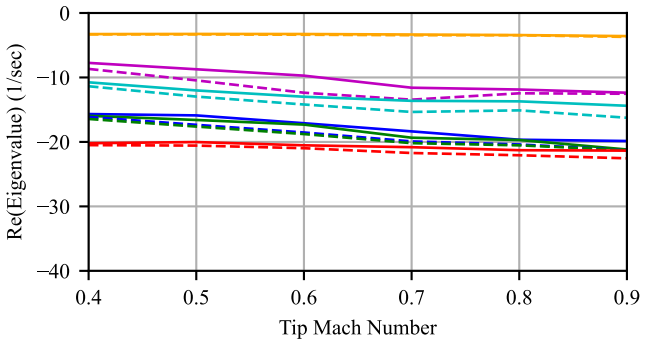

Figure 18. Real eigenvalue components vs M_{tip}, ρ = 0.013 kg/m^3, θ_{75} = 20 deg.

Figures 19-20 show stability versus collective for two different tip speeds: M_{tip} = 0.5 and 0.8. As with the constant coefficient analysis, most of the modes exhibit decreasing stability with increasing collective.

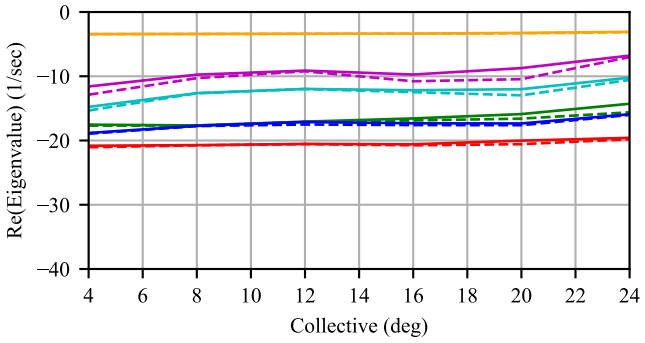

Figure 19. Real eigenvalue components vs collective, ρ = 0.013 kg/m^3, M_{tip} = 0.5.

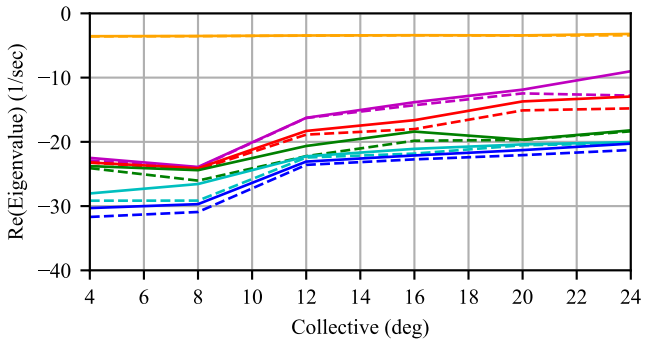

Figure 20. Real eigenvalue components vs collective, ρ = 0.013 kg/m^3, M_{tip} = 0.8.

All Blades | Dynamic Inflow | No Airframe DOF
Flutter Analysis: Floquet Theory

The analysis of the previous section was repeated but with the analysis of all blades and dynamic inflow. As with the prior section, lines of the same color are for the same mode. However, whereas the independent blade analysis of the previous section yielded two lines per mode (one per rotor) the inclusion of all blades in the analysis of the present section yields four lines per mode (one line per blade for each rotor). For each mode, the two lines corresponding to the smaller magnitude real eigenvalue components at the initial sweep condition are plotted with solid lines, while the other two are plotted with dashed lines.

The use of dynamic inflow yielded six additional eigenvalues; however, the real eigenvalue components for these modes are negative and of sufficient magnitude to be below the lowest bounds of the y-axes in Figures 21-24. The fact that the dynamic inflow modes have real eigenvalues very separated from those of the blade modes generally implies low coupling and little effect of dynamic inflow on blade mode stability. This insensitivity of the blade mode stability to the inclusion of dynamic inflow is observable through a comparison of the stability results of this section (Figures 21-24) with the stability results of the previous section. Other than the number of lines per mode, the stability results of these two sections are nearly identical, suggesting that dynamic inflow and multiblade analysis have negligible impact on the stability analysis of the rotor system.

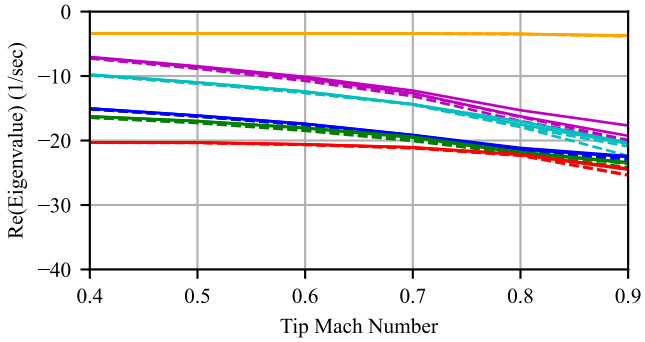

Figure 21. Real eigenvalue components vs M_{tip}, ρ = 0.013 kg/m^3, θ_{75} = 10 deg.

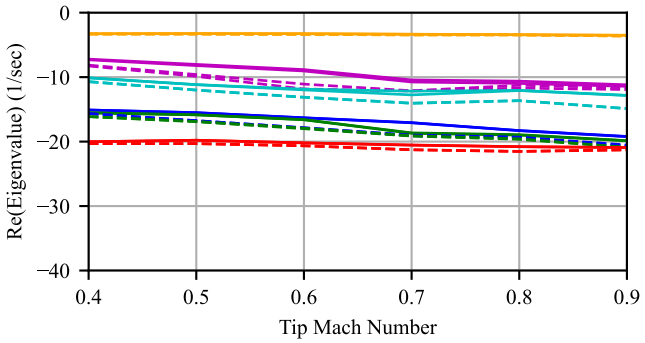

Figure 22. Real eigenvalue components vs M_{tip}, ρ = 0.013 kg/m^3, θ_{75} = 20 deg.

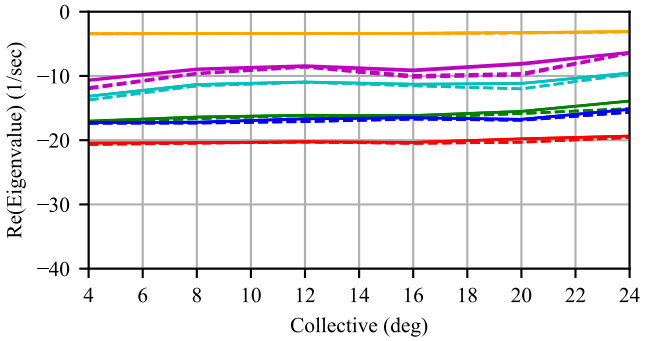

Figure 23. Real eigenvalue components vs collective, ρ = 0.013 kg/m^3, M_{tip} = 0.5.

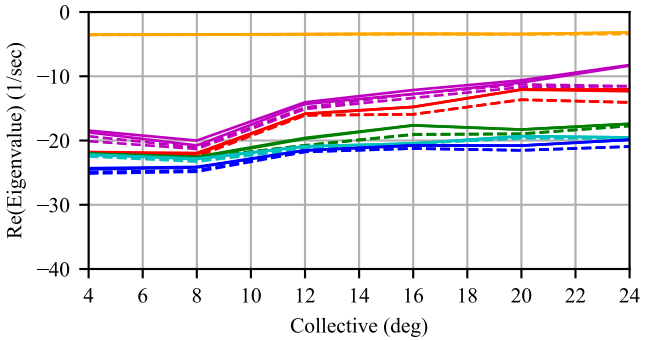

Figure 24. Real eigenvalue components vs collective, ρ = 0.013 kg/m^3, M_{tip} = 0.8.

All Blades | Dynamic Inflow | Airframe DOF Flutter Analysis: Floquet Theory

The analysis of the previous section was repeated, but with airframe rigid body degrees of freedom enabled. Activating the airframe degrees of freedom resulted in an additional eight eigenvalues, which are represented by the dotted black lines in Figures 25-28. Note that while the blade modes are stable, some of the airframe modes are unstable; however, this instability would be mitigated by the vehicle control system, which is not considered in the present work. As in the results of the previous subsection, the six dynamic inflow modes have real eigenvalue components that are negative and of sufficient magnitude to be below the lowest bounds of the y-axes in Figures 25-28.

Regarding rotor modes, as with the prior subsection, lines of the same color are for the same blade mode, and there are in general, four lines per mode – one for each blade. However, for some modes, such as the minimally damped rotor mode (yellow) in Figure 28, there are more than four lines. This is because in the eigenvalue analysis, most of the eigenvalues are in complex conjugate pairs (eight eigenvalues per mode, with four distinct real eigenvalue components to plot). However, for some modes (such as the yellow mode in Figure 28), the eight eigenvalues do not correspond to four complex conjugate pairs. In these cases, all distinct real eigenvalue components are plotted. The author's plotting convention for each mode was to plot as a solid line any distinct lines corresponding to the four eigenvalues of smallest magnitude real component at the initial sweep condition. All other distinct lines were plotted as dashed lines.

There does appear to be some level of coupling between some of the rotor modes and the airframe rigid body motion, most notable for the minimally damped lag mode depicted with yellow lines in Figures 25-28. For this mode, the multiple lines appear to split from one another when the airframe is introduced, a phenomenon not observed with the analysis of the previous subsection, which did not include the airframe modes. Nevertheless, the stability trends of this section are generally in agreement with those of the previous section, suggesting that inclusion of the airframe rigid body degrees of freedom is not crucial for understanding the overall stability of this rotor system but may be necessary to understand modal couplings.

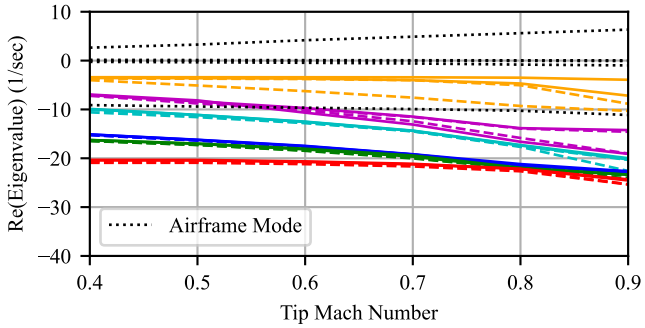

Figure 25. Real eigenvalue components vs M_{tip}, ρ = 0.013 kg/m^3, θ_{75} = 10 deg.

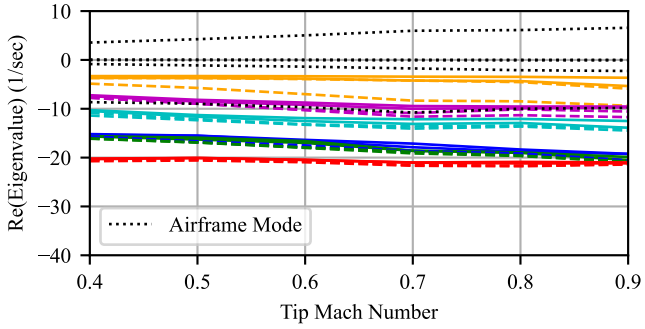

Figure 26. Real eigenvalue components vs M_{tip}, ρ = 0.013 kg/m^3, θ_{75} = 20 deg.

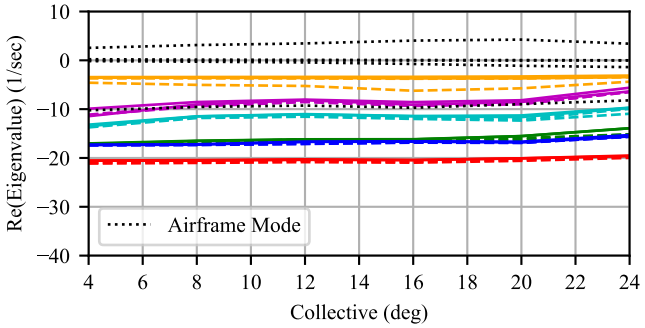

Figure 27. Real eigenvalue components vs collective, ρ = 0.013 kg/m^3, M_{tip} = 0.5.

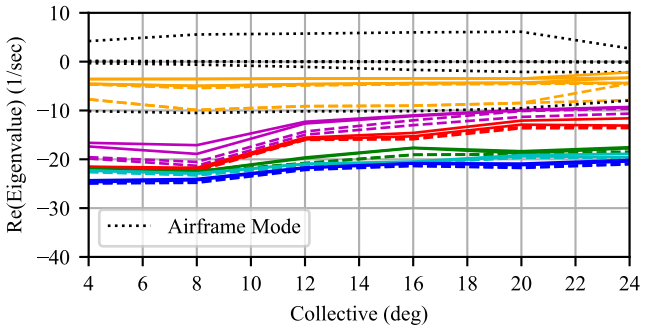

Figure 28. Real eigenvalue components vs collective, ρ = 0.013 kg/m^3, M_{tip} = 0.8.

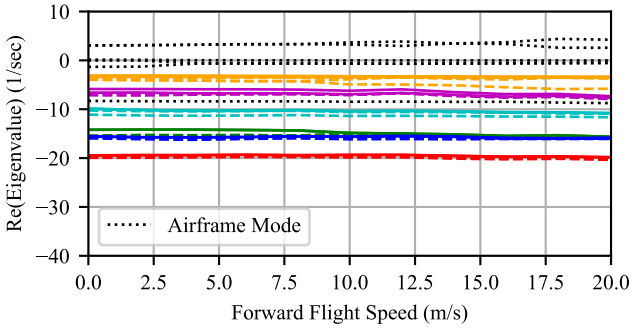

Figure 29. Real eigenvalue components vs flight speed, ρ = 0.013 kg/m^3, M_{tip} = 0.5.

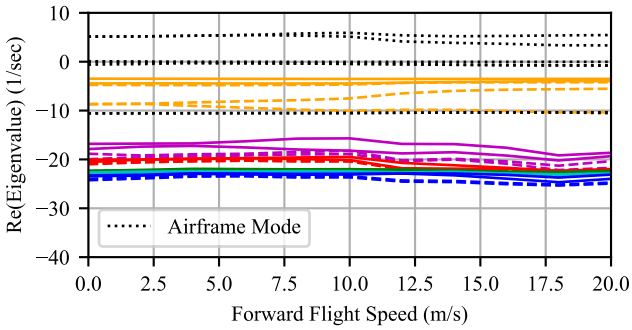

Figure 30. Real eigenvalue components vs flight speed, ρ = 0.013 kg/m^3, M_{tip} = 0.8.

SRH FORWARD FLIGHT RESULTS

This section is devoted to SRH forward flight analysis. Six degree of freedom trim was employed. Here, only the highest level of modeling (all blades, dynamic inflow, airframe rigid body degrees of freedom, and Floquet theory) was analyzed. The analysis presented is restricted to the 0.013 kg/m^3 condition.

Results are presented in Figures 29-30 for sweeps of forward flight speed for two different values of M_{tip}. A similar plotting scheme was used for these results as was used for the final subsection of hover results. Inflow modes are negative and of sufficient magnitude as to be below the minimum bounds of the y-axes in Figures 29-30.

Generally, the modes are fairly insensitive to forward flight speed. The only unstable modes, depicted by the black dotted lines, are from the airframe and are thus not of concern for the rotor design (other than for the evaluation of potential coupling with rotor modes). The airframe modes would be stabilized by the vehicle control system.

SRH ROTOR STRUCTURAL PARAMETER EXCURSIONS

As shown in the preceding sections, the SRH rotor as designed is stable within the expected operational envelope. The present section is devoted to results from analysis with off-design values for specific structural properties. The purpose of these parameter excursions was to identify conditions for aeroelastic instability of a rotor on Mars. Results for excursions of flap and torsion stiffness and chordwise center of gravity (CG) are presented.

For these excursions, a hover condition was analyzed with only the simplest modeling scheme (independent blade, trim inflow, no airframe degrees of freedom, and a constant coefficient flutter analysis). This is deemed sufficient for these exploratory cases, particularly considering the previously displayed relative insensitivity of SRH rotor stability to increased modeling fidelity.

A Set of Conditions for Dynamic Instability

Flap stiffness was reduced to 25% of the nominal SRH value, yielding an in vacuo first flap frequency of 1.4 per-rev at 2600 RPM (~M_{tip} = 0.8). Previous analysis was performed for a Mars rotor with a first flap frequency of 1.5 per-rev (Ref. 9), so this is not a wholly unrealistic value for flap stiffness. The rotor was stable at 2600 RPM, even with 25% flap stiffness.

With flap stiffness set to 25% of the nominal value and a rotor speed of 2600 RPM, torsion stiffness was swept by scaling the sectional values. Figure 31 displays modal frequencies and damping ratios plotted against fraction of nominal torsion stiffness. Dynamic instability is apparent with 81.5% torsion stiffness and corresponds to the convergence of the two lowest frequency modes.

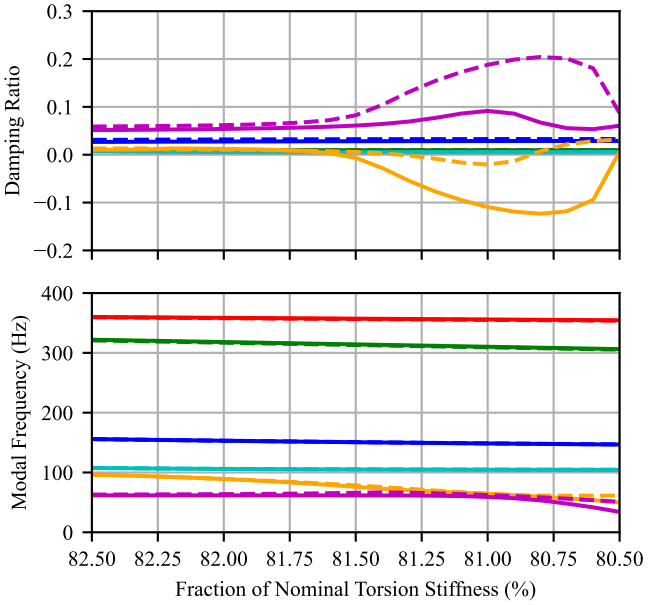

Figure 31. Modal frequencies and damping ratios vs fraction of nominal torsion stiffness, 25% flap stiffness, ρ = 0.013 kg/m^3, θ_{75} = 10 deg, rotor speed = 2600 RPM.

The results of the eigenvalue analysis suggest that with 25% nominal flap stiffness and 2600 RPM, 80% nominal torsion stiffness (beyond the x-axis of Figure 31) yields static divergence. However, with 25% flap stiffness, 80% torsion stiffness, and 2600 RPM, a sweep of chordwise CG location revealed dynamic instability. Figure 32 shows modal frequencies and damping ratios plotted against the offset of the chordwise CG from the nominal location. The CG offset values are given as fractions of local chord, with positive values indicating an aft offset from nominal. Figure 32 shows that the frequencies of the two lowest-frequency modes are converged with aft chordwise CG shifts of approximately 8% to 14% local chord. The frequency convergence of the two modes corresponds to the dynamic instability of the two modes displayed in the damping ratio plot in Figure 32.

While not representative of the actual SRH rotor, the conditions in Figures 31-32 serve to demonstrate the potential for dynamic instabilities of rotors in the Martian environment if blade structural properties are not chosen appropriately.

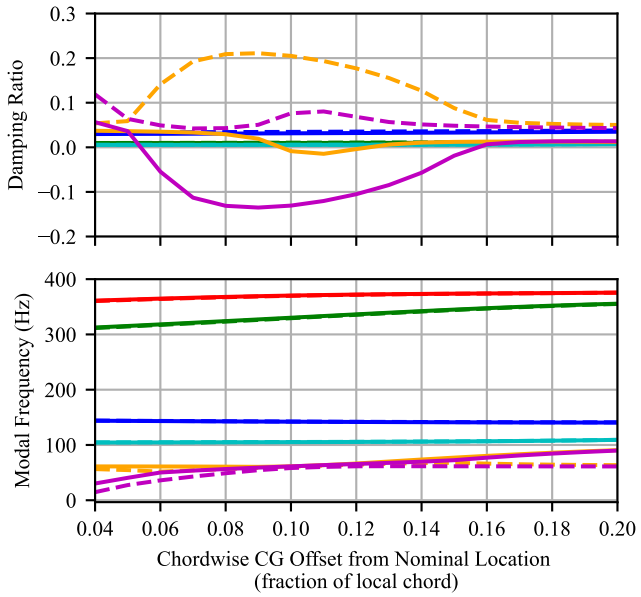

Figure 32. Modal frequencies and damping ratios vs chordwise CG offset, 25% flap stiffness, 80% torsion stiffness, ρ = 0.013 kg/m^3, θ_{75} = 10 deg, rotor speed = 2600 RPM.

CONCLUSIONS

The following general conclusions are drawn:

1. Both the SRH and Ingenuity rotors are stable for the analyzed conditions, which were chosen to be representative of operational conditions on Mars.

2. Analysis of an independent blade, in hover, with trim inflow, and without the inclusion of airframe degrees of freedom shows the principal dependence of aeroelastic stability on operating conditions (density, rotor speed, and collective). Dynamic inflow, airframe motion, and forward flight (requiring Floquet theory for analysis) had little influence on the rotor aeroelastic stability.

3. Dynamic instabilities can be encountered for Martian rotors, given certain settings of blade structural parameters. In the present work, flap stiffness, torsion stiffness, and chordwise CG location were explored, revealing the destabilizing effects of decreased stiffness and the sensitivity of the reduced-stiffness rotor stability to chordwise CG location. Other structural parameters may have similar stability-altering effects. Care must be taken during the blade design process to ensure that the structural design offers stability throughout the operational envelope.

Throughout this work, stability results were generated, and trends were observed, documented, and discussed. Further work might include parameter variations to explore the reasons for differences and similarities between the SRH and Ingenuity rotor systems. Parameter variation studies could also lead to further understanding of the causes behind the

observed effects of rotor speed and collective on rotor stability.

Author contact: Stephen Wright stephen.j.wright@nasa.gov

ACKNOWLEDGMENTS

The Mars Sample Recovery Helicopters program is a joint effort between NASA Ames Research Center, NASA Langley Research Center, NASA's Jet Propulsion Laboratory, and AeroVironment, Inc.

The authors acknowledge the Mars Sample Return program, NASA's Jet Propulsion Laboratory, NASA Ames Research Center, NASA Langley Research Center, AeroVironment, Inc., and the NASA Convergent Aeronautics Solutions (CAS) Project for funding and support of this work.

The decision to implement Mars Sample Return will not be finalized until NASA's completion of the National Environmental Policy Act (NEPA) process. This document is being made available for information purposes only.

REFERENCES

1. Mars Exploration Program and the Jet Propulsion Laboratory, "Mars Helicopter Flight Log," NASA, dated April 26, 2023, https://mars.nasa.gov/technology/helicopter (accessed January 10, 2024).
2. Withrow-Maser, S., Cummings, H., Johnson, W., Malpica, C., Meyn, L., Schatzman, N., Young, L., Keennon, M., Pipenberg, B., Grip, H., Tzanetos, T., Allan, B., Chan, A., Koning, W., Ruan, A., "Mars Sample Recovery Helicopter: Rotorcraft to Retrieve the First Samples from the Martian Surface", Presented at the Vertical Flight Society's 79th Annual Forum & Technology Display, West Palm Beach, FL, May 16–18, 2023.
3. Mier-Hicks, F., Grip, H. F., Kalantari, A., Moreland, S., Pipenberg, B., Keennon, M., Canham, T. K., Pauken, M., Decrossas, E., Tzanetos, T., Balaram, J. B., "Sample Recovery Helicopter," 2023 IEEE Aerospace Conference, Big Sky, MT, March 2023.
4. Johnson, W., "Rotorcraft Aeromechanics Applications of a Comprehensive Analysis," HeliJapan 1998: AHS International Meeting on Rotorcraft Technology and Disaster Relief, Gifu, Japan, April 1998.
5. Klausmeier, C. A., "Floquet theory: a useful tool for understanding nonequilibrium dynamics," *Theoretical Ecology* 1, 153–161, 2008.
6. Koning, W. J. F., Johnson, W., Grip, H. F., "Improved Mars Helicopter Aerodynamic Rotor Model for Comprehensive Analyses," Presented at the 44th European Rotorcraft Forum, Delft, the Netherlands, September 18-21, 2018.
7. Pipenberg, B. T., Keennon, M. T., Tyler, J. D., Langberg, S. A., Hibbs, B., Balaram, J. B., Grip, H. F., Pempejian, J., "Design and Fabrication of the Mars Helicopter Rotor, Airframe, and Landing Gear Systems," AIAA SciTech Forum, San Diego, CA, USA, January 7-11, 2019.
8. Pipenberg, B. T., Keennon, M. T., Langberg, S. A., Tyler, J. D., "Development of the Mars Helicopter Rotor System," Presented at the Vertical Flight Society's 75th Annual Forum & Technology Display, Philadelphia, PA, USA, May 13-16, 2019.
9. Lumba, R., Cheng, C., Datta, A., Koning, W. J. F., Perez Perez, N., Cummings, H., "Structural Design and Aeromechanical Analysis of Unconventional Blades for Future Mars Rotorcraft," Presented at the Vertical Flight Society's Aeromechanics for Advanced Vertical Flight Technical Meeting, San Jose, CA, Jan 25-27, 2022.

APPENDIX A
SRH HOVER RESULTS, 0.020 KG/M^3

Independent Blade | Trim Inflow | No Airframe DOF
Flutter Analysis: Constant Coefficient

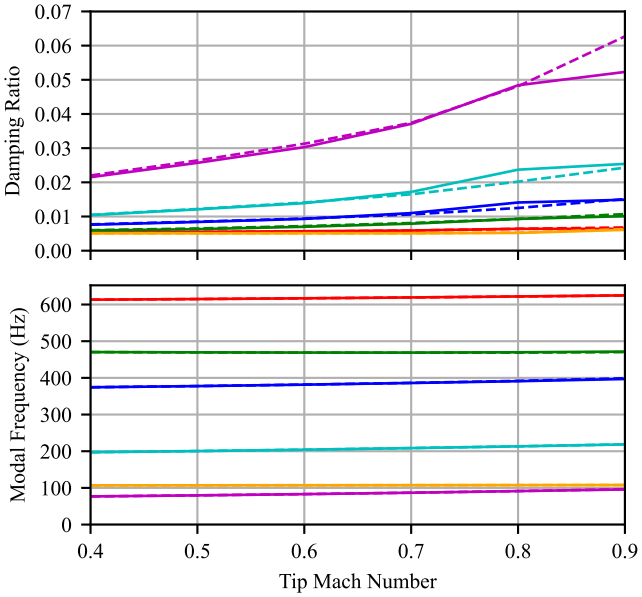

Figure A1. Modal frequency and damping vs M_{tip}, ρ = 0.020 kg/m^3, θ_{75} = 10 deg.

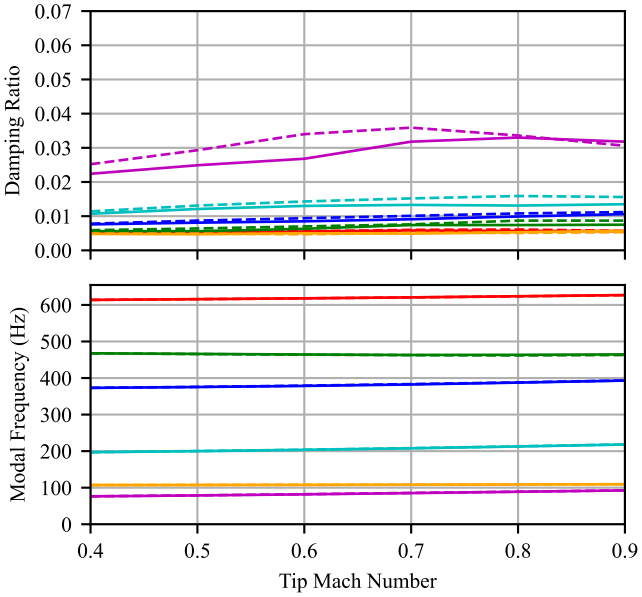

Figure A2. Modal frequency and damping vs M_{tip}, ρ = 0.020 kg/m^3, θ_{75} = 20 deg.

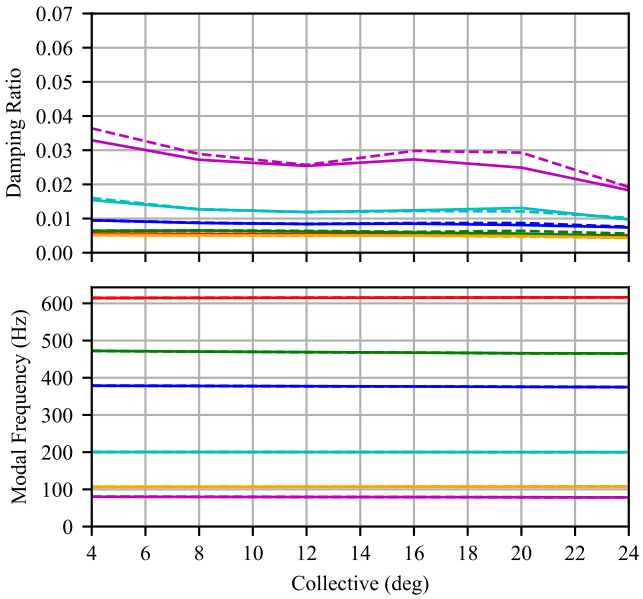

Figure A3. Modal frequency and damping vs collective, ρ = 0.020 kg/m^3, M_{tip} = 0.5.

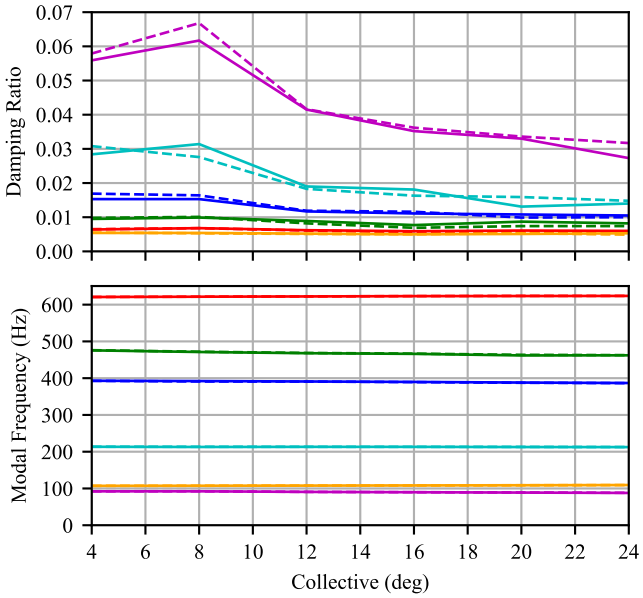

Figure A4. Modal frequency and damping vs collective, ρ = 0.020 kg/m^3, M_{tip} = 0.8.

Independent Blade | Trim Inflow | No Airframe DOF
Flutter Analysis: Floquet Theory

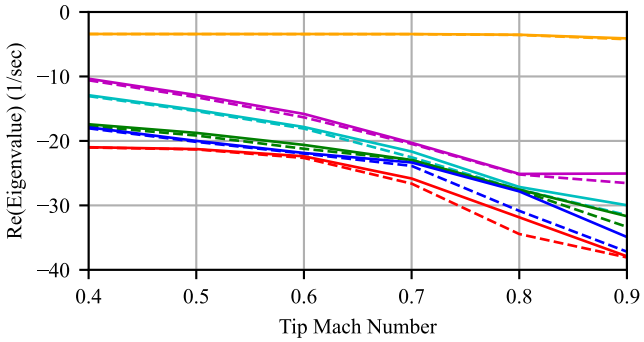

Figure A5. Real eigenvalue components vs M_{tip}, ρ = 0.020 kg/m^3, θ_{75} = 10 deg.

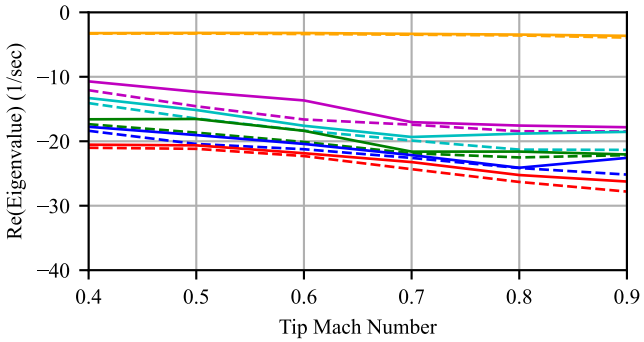

Figure A6. Real eigenvalue components vs M_{tip}, ρ = 0.020 kg/m^3, θ_{75} = 20 deg.

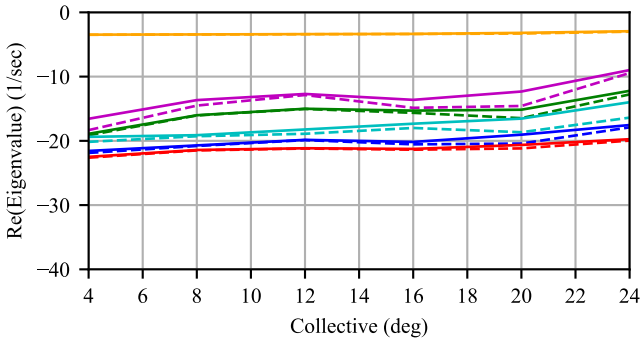

Figure A7. Real eigenvalue components vs collective, ρ = 0.020 kg/m^3, M_{tip} = 0.5.

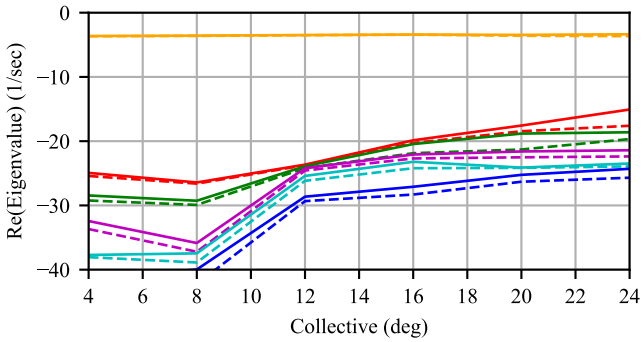

Figure A8. Real eigenvalue components vs collective, ρ = 0.020 kg/m^3, M_{tip} = 0.8.

All Blades | Dynamic Inflow | No Airframe DOF
Flutter Analysis: Floquet Theory

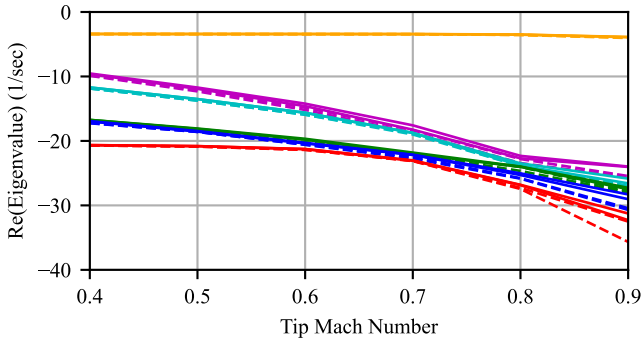

Figure A9. Real eigenvalue components vs M_{tip}, ρ = 0.020 kg/m^3, θ_{75} = 10 deg.

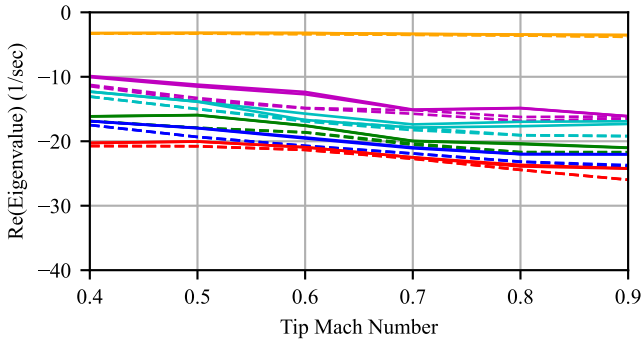

Figure A10. Real eigenvalue components vs M_{tip}, ρ = 0.020 kg/m^3, θ_{75} = 20 deg.

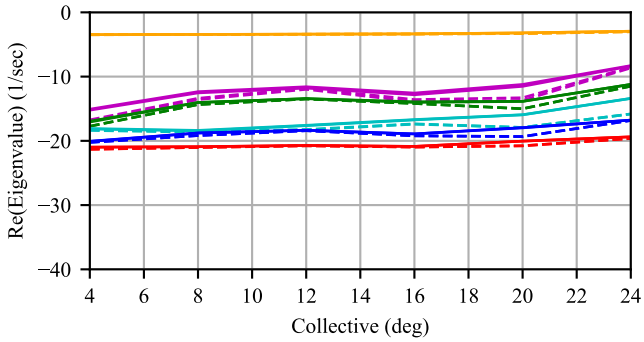

Figure A11. Real eigenvalue components vs collective, ρ = 0.020 kg/m^3, M_{tip} = 0.5.

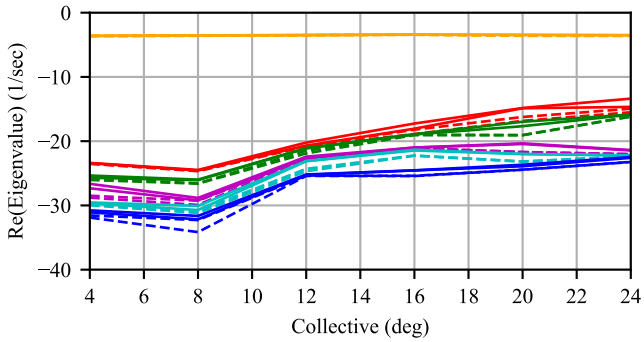

Figure A12. Real eigenvalue components vs collective, ρ = 0.020 kg/m^3, M_{tip} = 0.8.

All Blades | Dynamic Inflow | Airframe DOF
Flutter Analysis: Floquet Theory

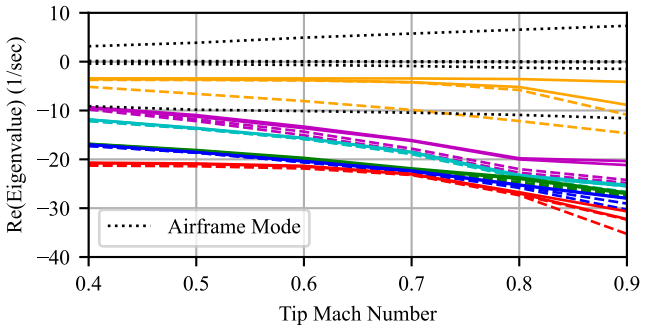

Figure A13. Real eigenvalue components vs M_{tip}, ρ = 0.020 kg/m^3, θ_{75} = 10 deg.

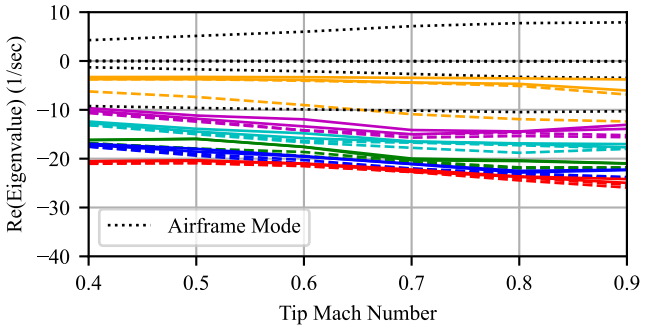

Figure A14. Real eigenvalue components vs M_{tip}, ρ = 0.020 kg/m^3, θ_{75} = 20 deg.

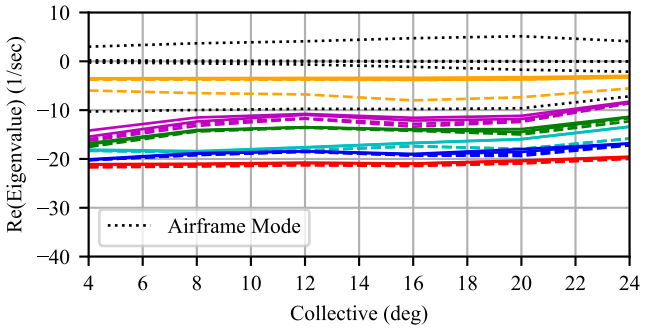

Figure A15. Real eigenvalue components vs collective, ρ = 0.020 kg/m^3, M_{tip} = 0.5.

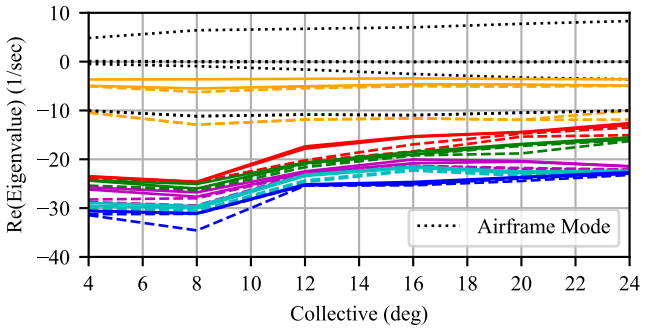

Figure A16. Real eigenvalue components vs collective, ρ = 0.020 kg/m^3, M_{tip} = 0.8.

APPENDIX B.
INGENUITY HOVER RESULTS

Independent Blade | Trim Inflow | No Airframe DOF
Flutter Analysis: Constant Coefficient

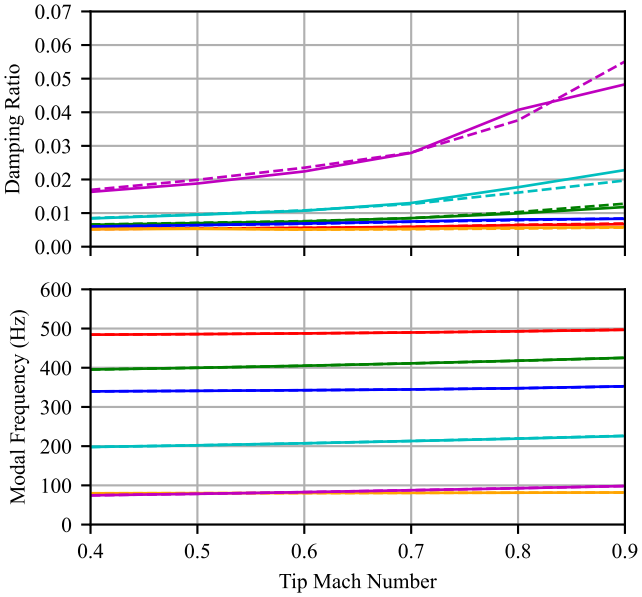

Figure B1. Modal frequency and damping vs M_{tip}, ρ = 0.013 kg/m^3, θ_{75} = 10 deg.

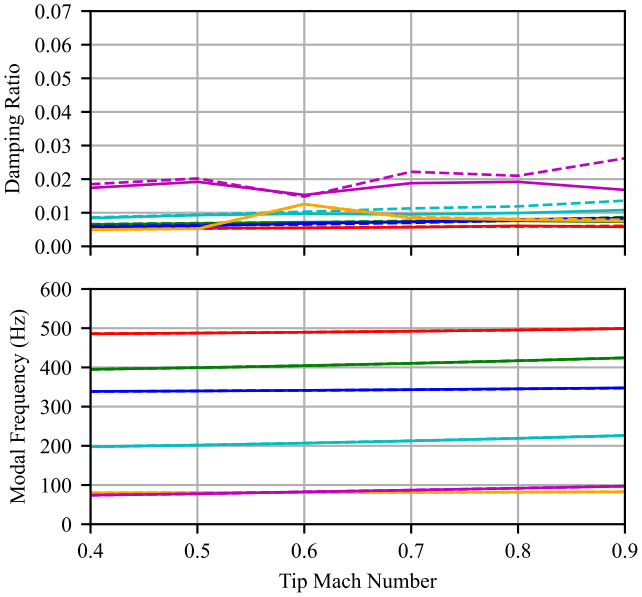

Figure B2. Modal frequency and damping vs M_{tip}, ρ = 0.013 kg/m^3, θ_{75} = 20 deg.

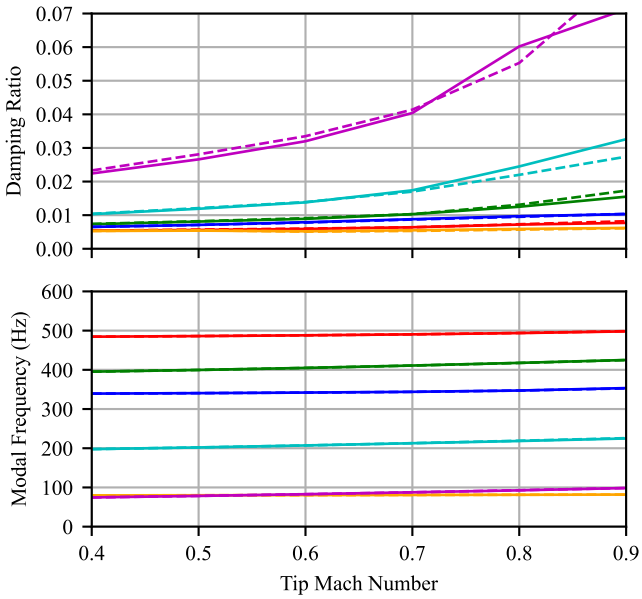

Figure B3. Modal frequency and damping vs M_{tip}, ρ = 0.020 kg/m^3, θ_{75} = 10 deg.

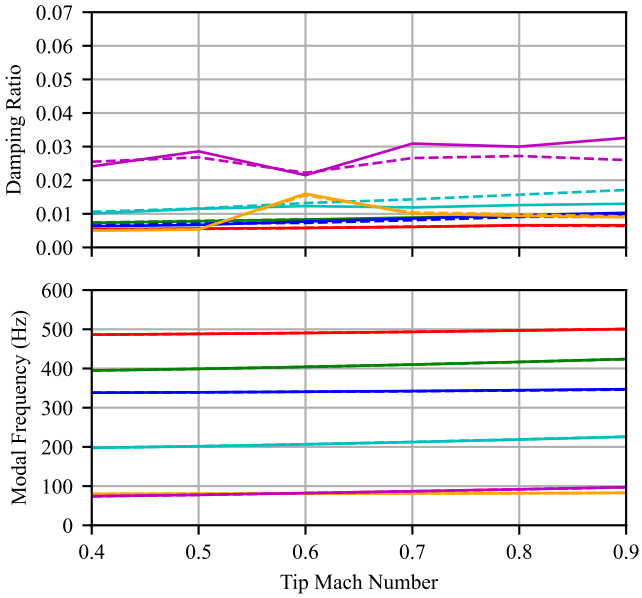

Figure B4. Modal frequency and damping vs M_{tip}, ρ = 0.020 kg/m^3, θ_{75} = 20 deg.

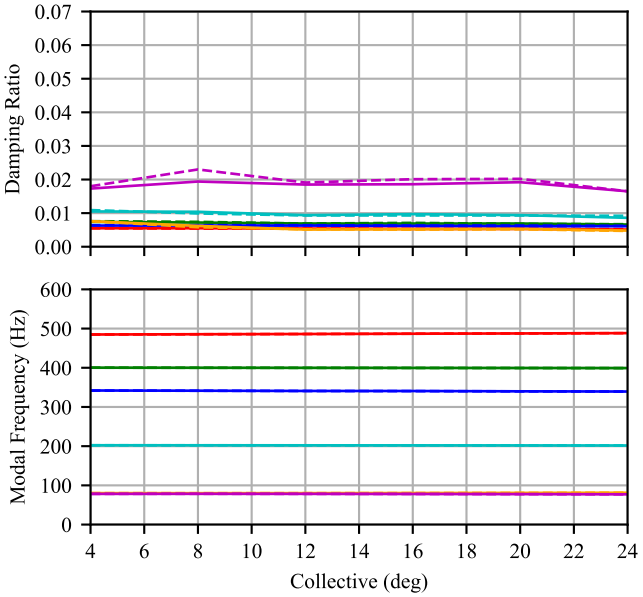

Figure B5. Modal frequency and damping vs collective, ρ = 0.013 kg/m^3, M_{tip} = 0.5.

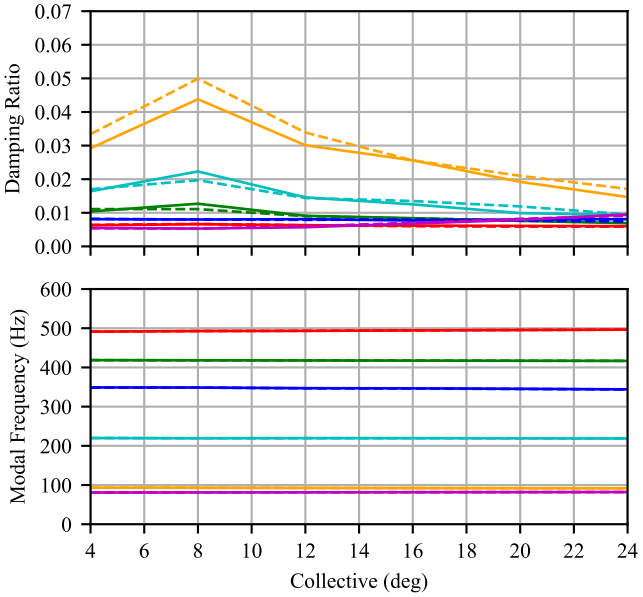

Figure B6. Modal frequency and damping vs collective, ρ = 0.013 kg/m^3, M_{tip} = 0.8.

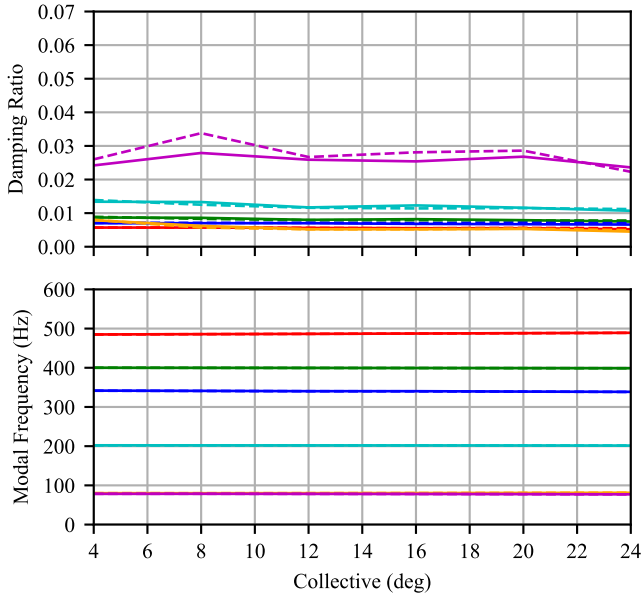

Figure B7. Modal frequency and damping vs collective, ρ = 0.020 kg/m^3, M_{tip} = 0.5.

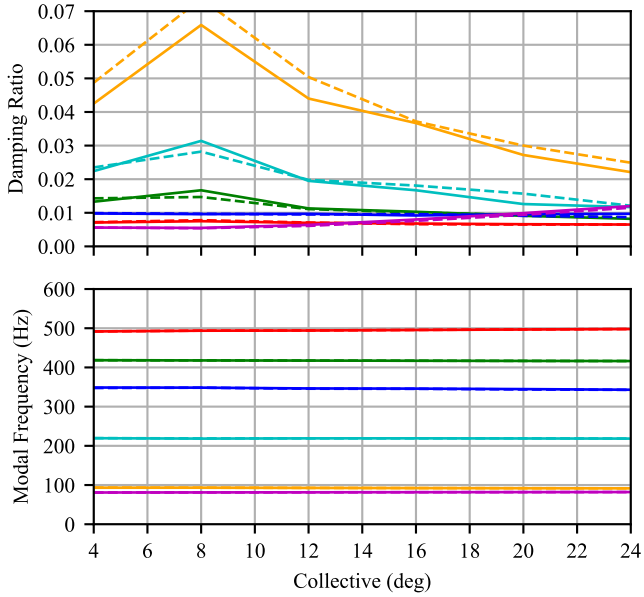

Figure B8. Modal frequency and damping vs collective, ρ = 0.020 kg/m^3, M_{tip} = 0.8.

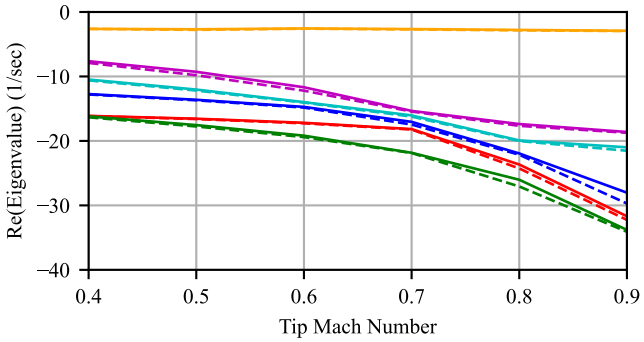

Figure B9. Real eigenvalue components vs M_{tip}, ρ = 0.013 kg/m^3, θ_{75} = 10 deg.

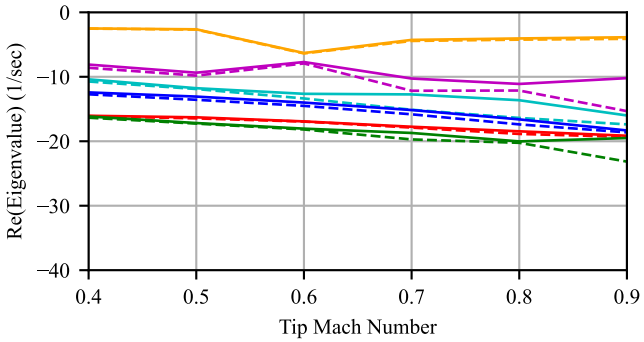

Figure B10. Real eigenvalue components vs M_{tip}, ρ = 0.013 kg/m^3, θ_{75} = 20 deg.

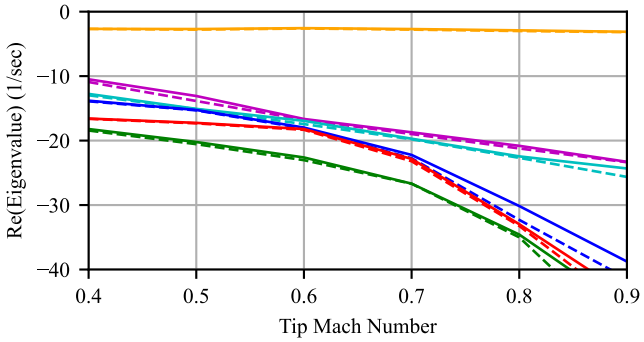

Figure B11. Real eigenvalue components vs M_{tip}, ρ = 0.020 kg/m^3, θ_{75} = 10 deg.

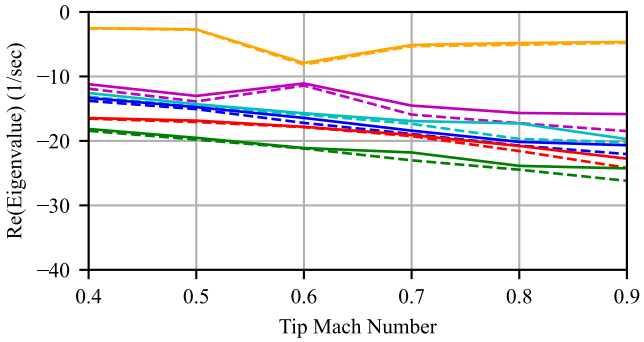

Figure B12. Real eigenvalue components vs M_{tip}, ρ = 0.020 kg/m^3, θ_{75} = 20 deg.

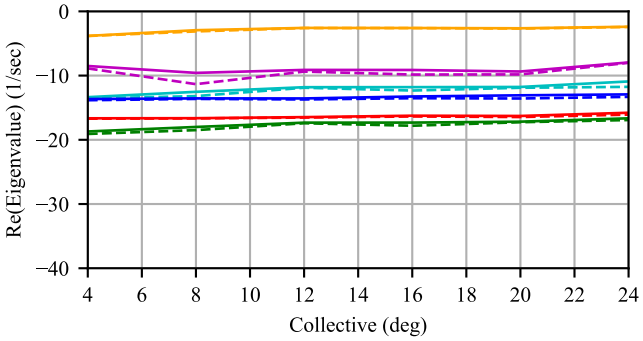

Figure B13. Real eigenvalue components vs collective, ρ = 0.013 kg/m^3, M_{tip} = 0.5.

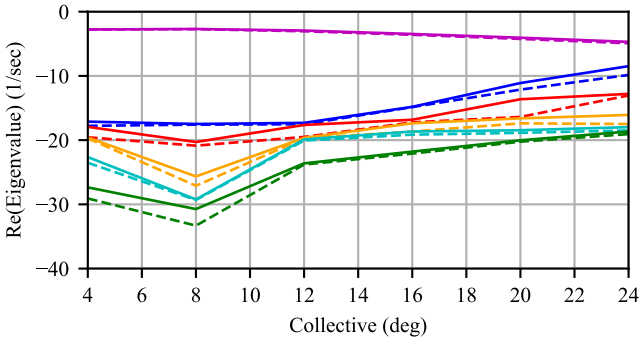

Figure B14. Real eigenvalue components vs collective, ρ = 0.013 kg/m^3, M_{tip} = 0.8.

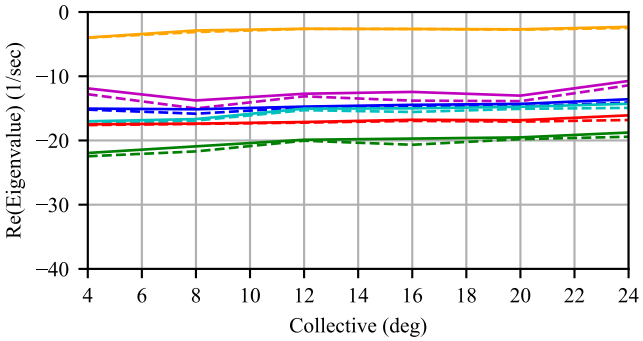

Figure B15. Real eigenvalue components vs collective, ρ = 0.020 kg/m^3, M_{tip} = 0.5.

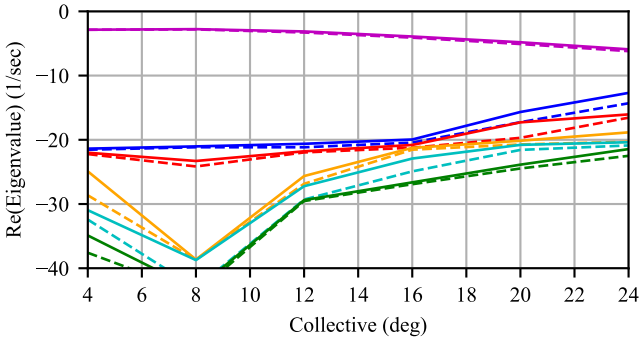

Figure B16. Real eigenvalue components vs collective, ρ = 0.020 kg/m^3, M_{tip} = 0.8.

All Blades | Dynamic Inflow | No Airframe DOF
Flutter Analysis: Floquet Theory

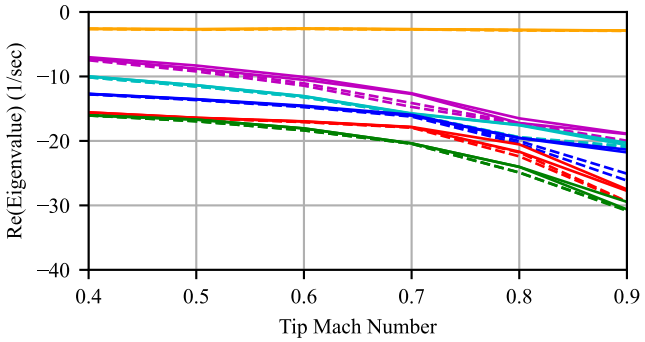

Figure B17. Real eigenvalue components vs M_{tip}, ρ = 0.013 kg/m^3, θ_{75} = 10 deg.

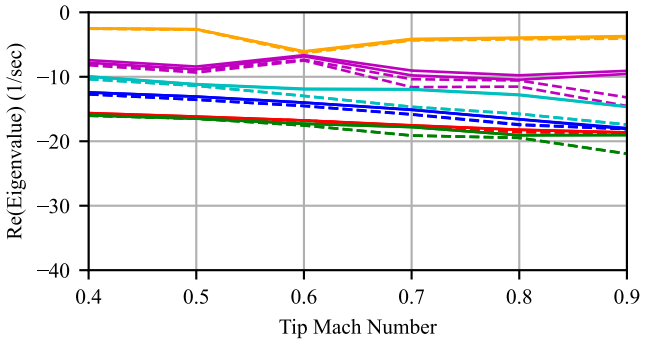

Figure B18. Real eigenvalue components vs M_{tip}, ρ = 0.013 kg/m^3, θ_{75} = 20 deg.

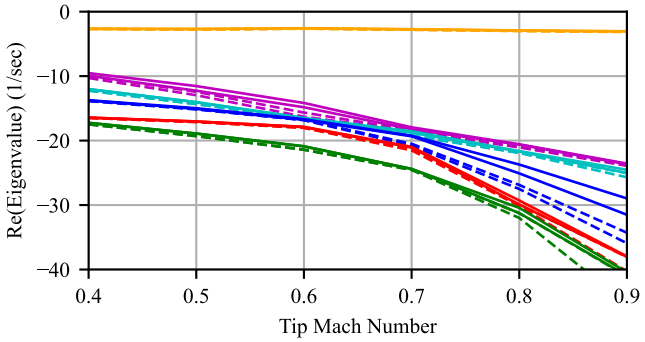

Figure B19. Real eigenvalue components vs M_{tip}, ρ = 0.020 kg/m^3, θ_{75} = 10 deg.

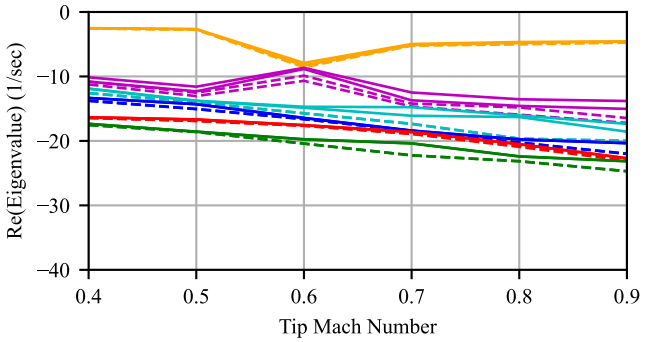

Figure B20. Real eigenvalue components vs M_{tip}, ρ = 0.020 kg/m^3, θ_{75} = 20 deg.

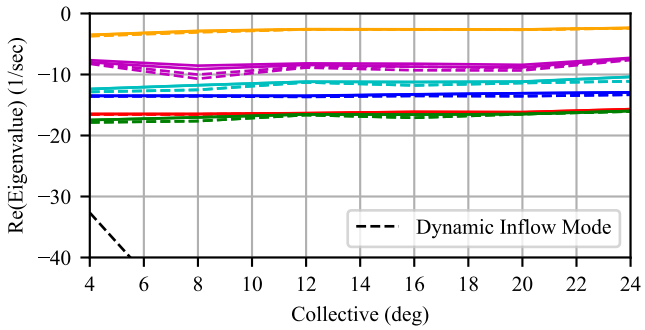

Figure B21. Real eigenvalue components vs collective, ρ = 0.013 kg/m^3, M_{tip} = 0.5.

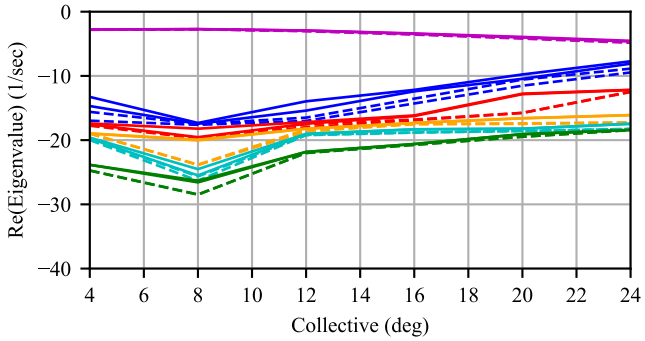

Figure B22. Real eigenvalue components vs collective, ρ = 0.013 kg/m^3, M_{tip} = 0.8.

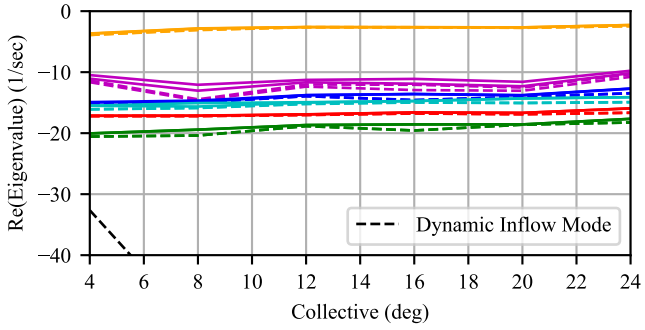

Figure B23. Real eigenvalue components vs collective, ρ = 0.020 kg/m^3, M_{tip} = 0.5.

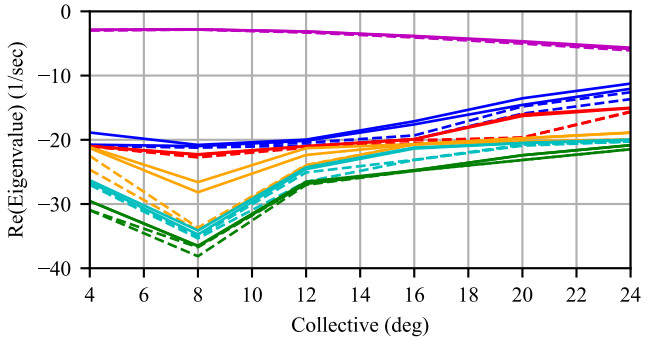

Figure B24. Real eigenvalue components vs collective, ρ = 0.020 kg/m^3, M_{tip} = 0.8.

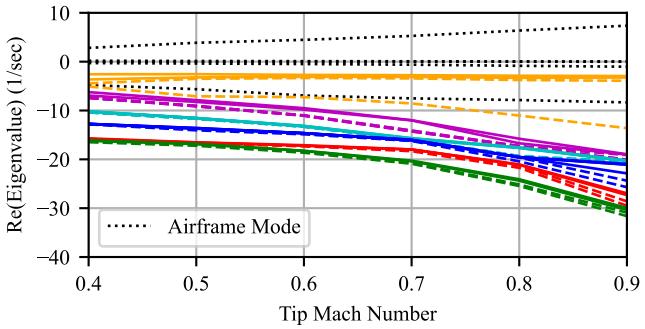

Figure B25. Real eigenvalue components vs M_{tip}, ρ = 0.013 kg/m^3, θ_{75} = 10 deg.

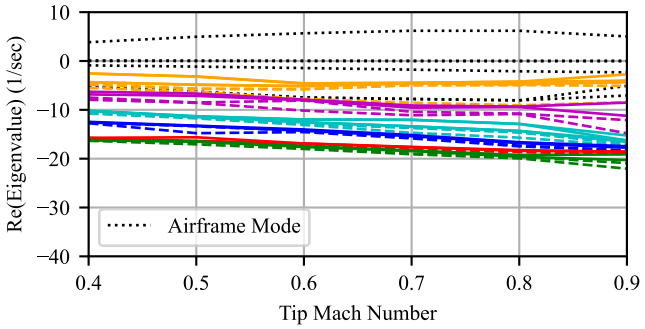

Figure B26. Real eigenvalue components vs M_{tip}, ρ = 0.013 kg/m^3, θ_{75} = 20 deg.

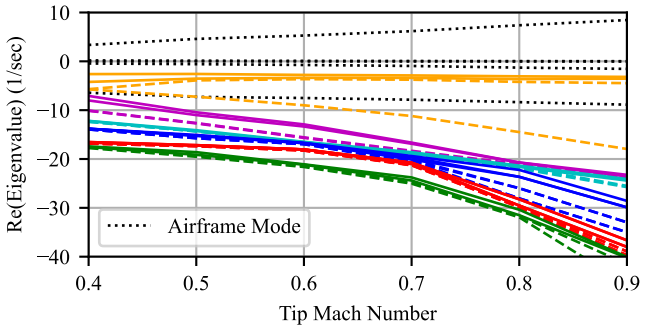

Figure B27. Real eigenvalue components vs M_{tip}, ρ = 0.020 kg/m^3, θ_{75} = 10 deg.

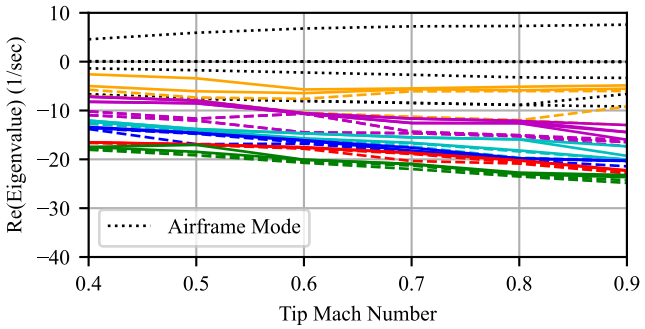

Figure B28. Real eigenvalue components vs M_{tip}, ρ = 0.020 kg/m^3, θ_{75} = 20 deg.

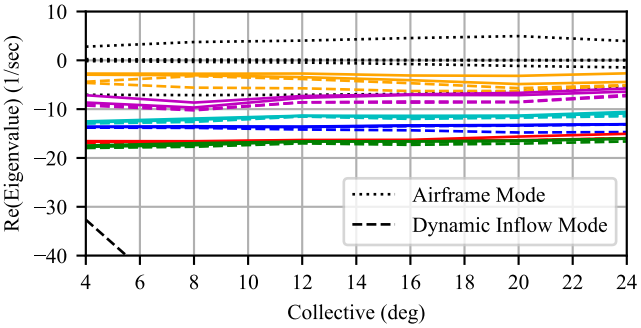

Figure B29. Real eigenvalue components vs collective, ρ = 0.013 kg/m^3, M_{tip} = 0.5.

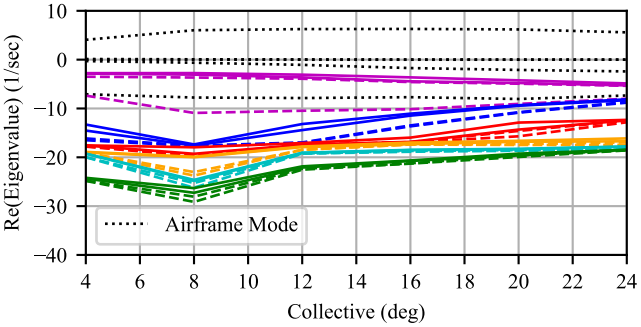

Figure B30. Real eigenvalue components vs collective, ρ = 0.013 kg/m^3, M_{tip} = 0.8.

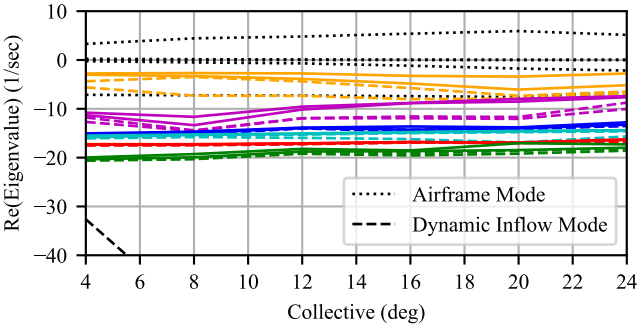

Figure B31. Real eigenvalue components vs collective, ρ = 0.020 kg/m^3, M_{tip} = 0.5.

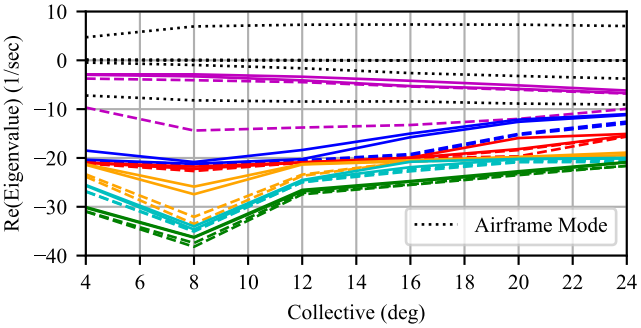

Figure B32. Real eigenvalue components vs collective, ρ = 0.020 kg/m^3, M_{tip} = 0.8.